Boise State University

ScholarWorks

Materials Science and Engineering Faculty Publications and Presentations

Micron School for Materials Science and Engineering

12-2019

Oxidation Behavior of Welded Zry-3, Zry-4, and Zr–1Nb Tubes

Jordan Vandegrift
Boise State University

Clemente J. Parga
Idaho National Laboratory

Ben Coryell
Idaho National Laboratory

Darryl P. Butt
Boise State University

Brian J. Jaques
Boise State University

Publication Information

Vandegrift, Jordan; Parga, Clemente J.; Coryell, Ben; Butt, Darryl P.; and Jaques, Brian J. (2019). "Oxidation Behavior of Welded Zry-3, Zry-4, and Zr–1Nb Tubes". *Nuclear Materials and Energy, 21*, 100714-1 - 100714-12. https://doi.org/10.1016/j.nme.2019.100714

Nuclear Materials and Energy 21 (2019) 100714

Contents lists available at ScienceDirect

Nuclear Materials and Energy

journal homepage: www.elsevier.com/locate/nme

Oxidation behavior of welded Zry-3, Zry-4, and Zr–1Nb tubes

Jordan Vandegrift[a,b,*], Clemente J. Parga[c], Ben Coryell[c], Darryl P. Butt[a,b], Brian J. Jaques[a,b]

[a] *Boise State University, 1910 W. University Dr., Boise, ID 83725, United States*
[b] *Center for Advanced Energy Studies, 995 University Blvd, Idaho Falls, ID 83401, United States*
[c] *Idaho National Laboratory, 2525 Fremont Ave, Idaho Falls, ID 83402, United States*

ARTICLE INFO

Keywords:
Zirconium alloys
Cladding
Breakaway
Transient
Oxidation

ABSTRACT

The Transient Reactor Test (TREAT) facility is a research reactor designed to simulate rapid transients to test new fuel designs. TREAT's cladding is exposed to unique conditions compared to normal water reactors. These conditions include: exposure to air at high temperatures (≥600 °C), rapid heating (≈700 $^{\circ C}/_{s}$), and cladding geometry that includes chamfers and welds. This work investigates the effects of chamfering and welding on the oxidation behavior of zirconium alloys (Zircaloy-3, Zircaloy-4, and Zr–1Nb). Tube specimens were examined under isothermal and transient conditions in dry and humid air. The effect of weld type (tungsten inert gas or electron beam), the number of welds, and alloying elements are compared. Thermogravimetric analysis was used to collect mass gain data during isothermal oxidation and the data was used to quantify the oxidation rate constant and the activation energy of oxidation. Oxide behavior in the weld region, chamfered region, and bulk tube was measured and compared. The microstructure and secondary phase precipitates in EBW tubes before and after breakaway were characterized. The electron beam welded Zr–1Nb specimen was found to have the most favorable oxidation behavior under both isothermal and transient conditions. Zry-4 oxidized the most readily and was the most affected by mechanical deformation.

1. Introduction

The Transient Reactor Test (TREAT) facility is a nuclear test facility at the Idaho National Laboratory (INL) which is designed to simulate a variety of transient type scenarios and provide safety data on new fuel designs. As part of an effort to convert TREAT from a highly enriched uranium fuel core to a low enriched uranium core, and because the legacy Zircaloy-3 (Zry-3) fuel cladding material is no longer commercially available, alternative zirconium alloys are being evaluated for use as cladding. It is important to understand the oxidation behavior of zirconium alloys, because it is the limiting factor for the maximum core temperature [1]. The oxidation behavior of zirconium alloys is not well studied in TREAT's conditions, which include: operation temperatures between 400–600 °C with an 820 °C design basis accident temperature (DBA), rapid transients up to 700 $^{\circ C}/_{s}$, and the use of air as coolant. Some literature is available on the behavior of zirconium alloys in these conditions; however, no studies have been completed to provide a direct comparison, with the same experimental parameters, of the alloys of interest. It has been shown that the corrosion resistance of zirconium alloys decreases with increasing temperature, and the oxidation reaction is thought to be catalyzed by the nitrogen present in air [2–4]. In a previous publication, the oxidation behavior of pure Zr, Zry-3, Zircaloy-4 (Zry-4), Zr–1Nb, and Zr–2.5Nb plate samples were systematically compared in both synthetic air and oxygen from 400–800 °C [5]. It was found that all four alloys experienced faster post-breakaway oxidation kinetics and had thicker, less protective oxides after oxidation in air compared to oxygen. Additionally, the Zr–1Nb oxidation kinetics were the slowest and it was the most resistant to the characteristic breakaway oxidation when compared to the Sn and Fe (Zry-3 and Zry-4) containing alloys [5].

TREAT's cladding differs from traditional cladding in that it has chamfers and welds (as seen in Fig. 1), both of which can alter the microstructure and, ultimately, the oxidation behavior of the fuel pin [6–8]. The grains in the weld region typically coarsen from the base metal towards the fusion zone, where the metal has experienced the highest temperature during welding [7].The grains in the base metal are usually equiaxed grains corresponding to α-Zr that coarsen in the heat affected zone (HAZ). In the fusion zone (FZ), the grains are found to be lamellar α-Zr [9]. Zhang et al. found that electron beam welded (EBW) Zr-702 (an Fe, Cr, and Hf containing alloy) had improved corrosion resistance in the weld region over the base metal due to dissolution of secondary phases during welding [9]. Cai et al. determined that weld beads formed using pulsed laser beam welding on a zirconium alloy containing Nb, Sn, and Fe spacer grid experienced excessive

---

[*] Corresponding author at: Boise State University, 1910 W. University Dr., Boise, ID 83725, United States.
E-mail address: jordanvandegrift@u.boisestate.edu (J. Vandegrift).

https://doi.org/10.1016/j.nme.2019.100714
Received 4 September 2019; Received in revised form 25 October 2019; Accepted 26 October 2019
Available online 19 November 2019
2352-1791/ © 2019 The Authors. Published by Elsevier Ltd. This is an open access article under the CC BY-NC-ND license
(http://creativecommons.org/licenses/BY-NC-ND/4.0/).

Fig. 1. Rendering of TREAT's unique fuel cladding assembly, which includes chamfered corners and welded end caps.

Table 1
Typical composition of zirconium alloys in wt% [24].

	Sn	Fe	Cr	O	Nb
Zry-3	0.25	0.25	–	–	–
Zry-4	1.5	0.21	0.1	0.13	–
Zr–1Nb	–	0.015–0.06	–	0.09–0.12	1

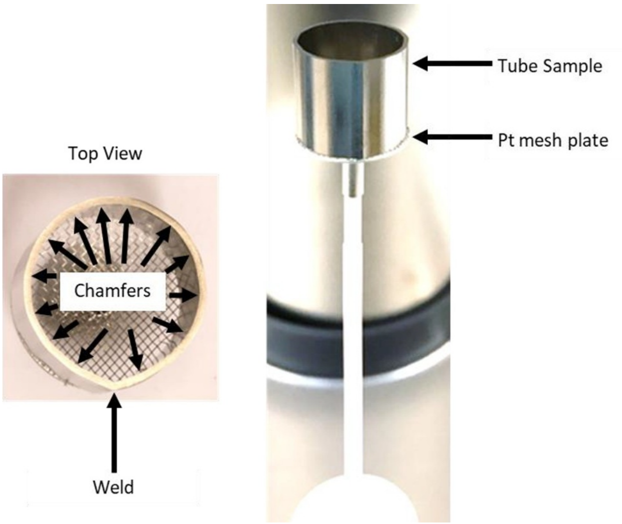

Fig. 2. Experimental setup inside the STA showing a welded tube specimen on the platinum mesh plate.

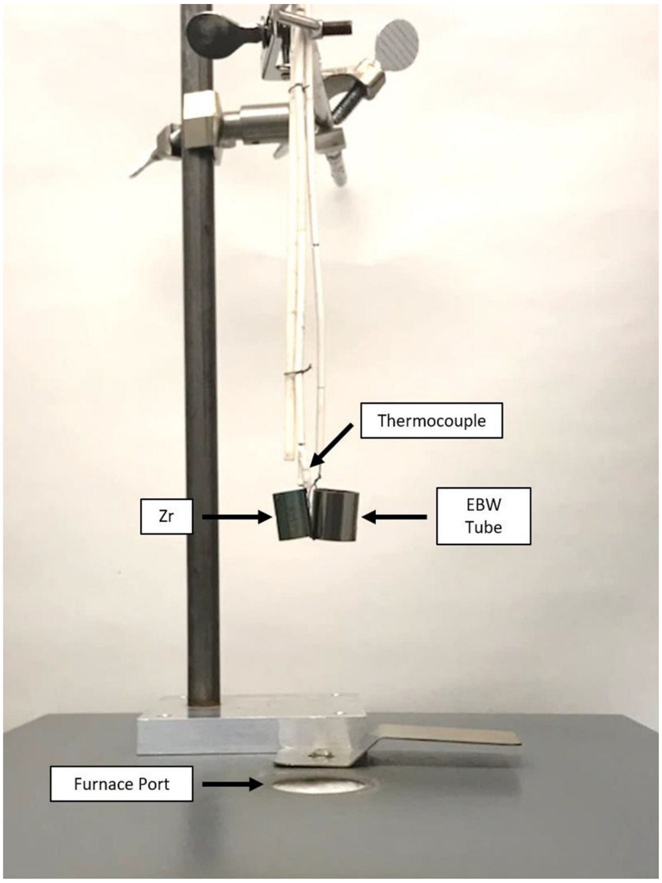

Fig. 4. Experimental setup for transient oxidation experiments. A pure Zr tube with a thermocouple spot welded to the surface was inserted into the furnace with the EBW zirconium alloy tube to monitor temperature during the experiment.

cracking compared to the base metal due to stresses at the metal/oxide interface [10]. Additionally, Ryabichenko et al. found that tungsten inert gas (TIG) welded Zr-Nb alloys had similar corrosion resistance to EBW alloys [11]. Although some studies on the oxidation behavior of

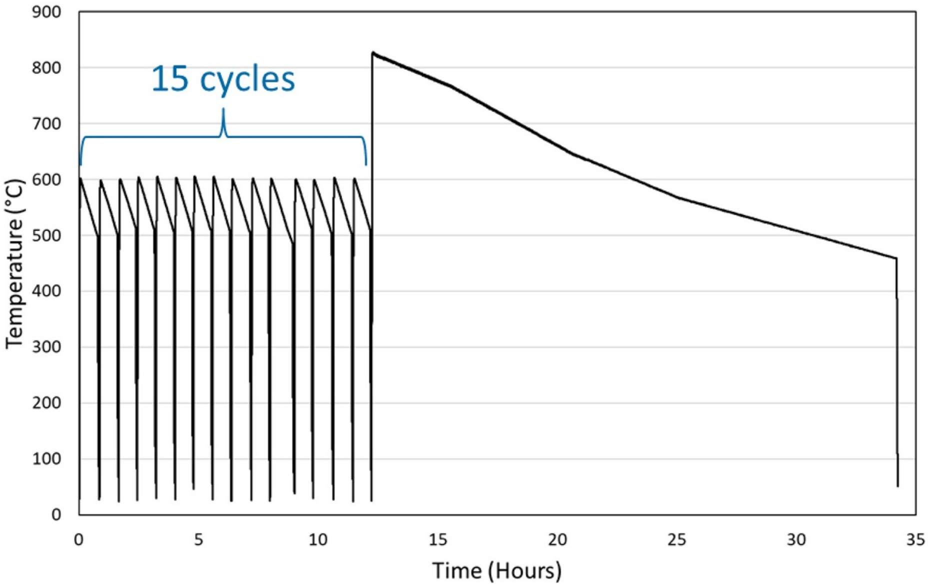

Fig. 3. Transient oxidation temperature profile followed for each sample showing fifteen transients from 600 to 500 °C simulating normal TREAT operation, followed by a DBA temperature profile from 820 to 450 °C.

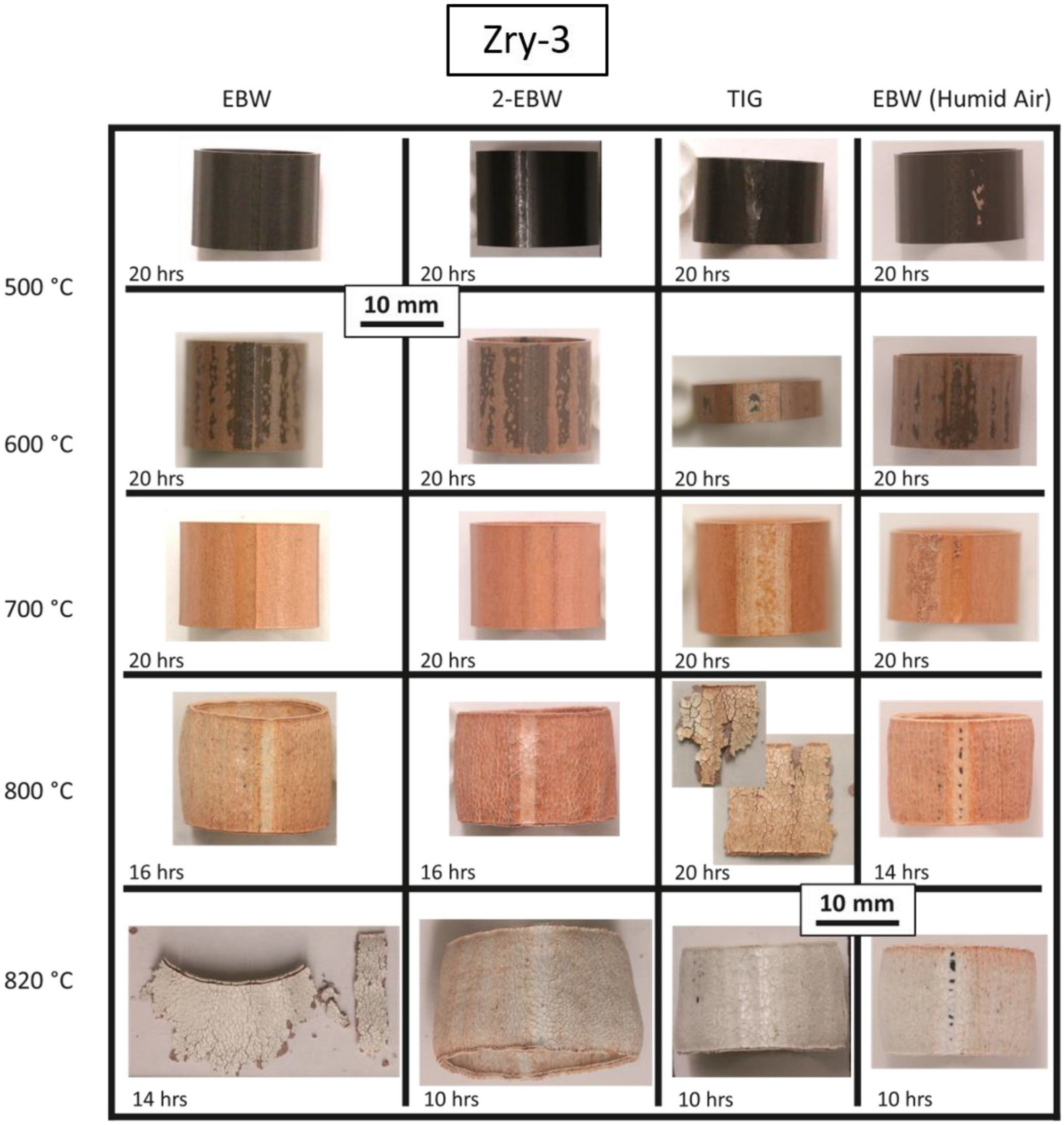

Fig. 5. Macroscopic images of Zry-3 EBW or TIG welded tubes after isothermal oxidation experiments in dry or humid air with the weld facing forward.

EBW and TIG welded zirconium alloys have been reported, none present a direct comparison of the oxidation of Zry-3, Zry-4, and Zr-1Nb welded tubes in TREAT's conditions.

Mechanical deformation (such as chamfering) affects the microstructure of the bulk metal, however, it is unclear how this affects the oxidation behavior of zirconium alloys. Plastic deformation has been shown to decrease the grain size and increase dislocation density of zirconium [12–14]. Modeling the oxidation of zirconium with various grain sizes indicates that corrosion resistance of zirconium increases with decreasing grain size before breakaway [15]. However, the model did not predict how grain size would affect the breakaway transition or the oxidation kinetics after breakaway. Additionally, only zirconium metal was modelled, alloying constituents were not considered. In a study by Rogachev et al., it was reported that plastic deformation via high pressure torsion creates stresses in the metal and results in phase transformation in zirconium [13]. Studies have reported that the oxidation behavior of zirconium varies with the phase of the metal. The room temperature α-Zr phase and β-Nb phase improve corrosion resistance, while the β-Zr phase is detrimental to corrosion resistance [16,17]. Although some studies have been reported on the effect of plastic deformation on the microstructure of zirconium, the effect of chamfering on the oxidation behavior Zry-3, Zry-4, and Zr–1Nb remains unclear.

This work is intended to provide a direct comparison between three candidate zirconium alloy cladding materials, Zry-3, Zry-4, and Zr–1Nb during both isothermal and rapid transient experiments in dry and humid air. The effects of welding, weld type, and chamfering on the oxidation kinetics are compared.

2. Experimental procedures

2.1. Materials

Zry-3, Zry-4, and Zr–1Nb tube samples were fabricated at the INL by plastically deforming sheets of material with 15 chamfers and welding the seam with either a single longitudinal EBW, two longitudinal EBW, or two longitudinal TIG welds. The tubes had an approximate diameter of 16 mm and the Zry-3 tubes had a wall thickness of 0.63 mm while Zry-4 and Zr-1Nb had wall thicknesses of 0.66 mm. Prior to oxidation, the tubes were subjected to an annealing heat treatment to remove

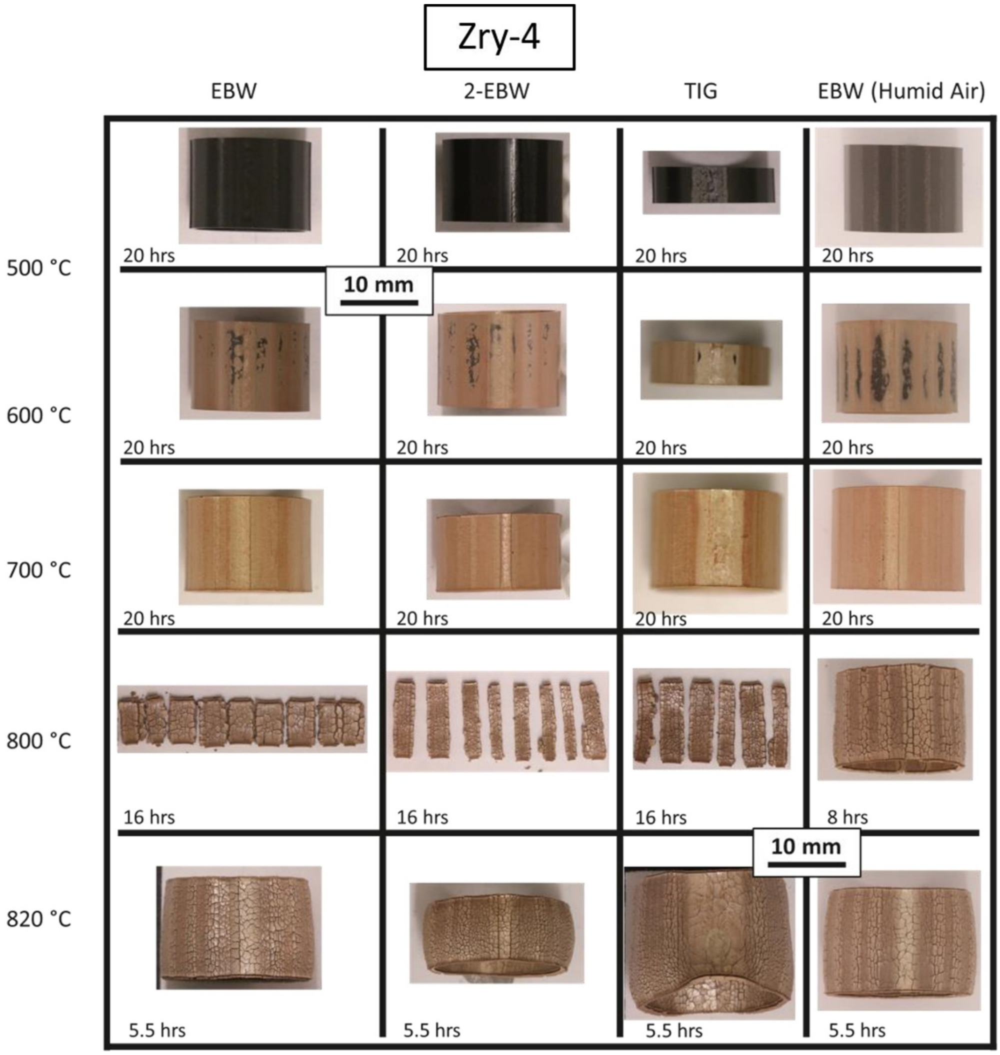

Fig. 6. Macroscopic images of Zry-4 EBW or TIG welded tubes after isothermal oxidation experiments in dry or humid air with the weld facing forward.

stresses present from fabrication. The annealing heat treatment included heating to 450 °C at 20 $^{\circ C}/_{min}$ ramp under high vacuum ($< 10^{-7}$ torr or 1.3×10^{-5} Pa) where they were held for 24 h before being cooled to room temperature at the same rate. The tubes were cleaned by sonication in a solution of 1:1:1 acetone:ethanol:deionized water before oxidation. The composition of the zirconium alloys is shown in Table 1.

2.2. Isothermal oxidation

Twenty-hour isothermal oxidation experiments in dry and humid synthetic air (certified N_2 + 20% O_2) were performed in a NETZSCH STA-449 F3 Jupiter equipped with thermogravimetric analysis (TGA). A platinum-mesh plate was used as a sample carrier to maximize the interaction of the sample with the reactant gasses as shown in Fig. 2. Humid air oxidation experiments were done with a partial pressure of water P_{H2O} = =0.29 psi or 1999.5 Pa (30% relative humidity at 37.8 °C or 100 °F), which is typical of the moisture content in the desert air during typical TREAT operation. The dry air oxidation experiments were performed on single EBW, double EBW (2-EBW), and TIG welded tubes. All isothermal oxidation experiments in the temperature range 500–700 °C were held for 20 h. Experiments done at 800 and 820 °C were shortened due to severe degradation of the specimens. After oxidation the mass gain data (normalized to the measured initial surface area of the tubes) was used to quantify the oxidation rate constants of each alloy at each temperature. The determined oxidation rates were then used to determine the activation energies for oxidation of each specimen.

The oxide thickness of the non-plastically deformed (bulk), chamfered, and welded regions were each measured after 20-hour isothermal oxidation at 700 °C. Only samples oxidized at 700 °C were measured because a direct comparison of oxidation behavior could be made, whereas the samples oxidized at higher temperatures were oxidized for various durations, as previously stated. The tubes were ground down approximately 2 mm from the top surface to image the metal/oxide interface using optical microscopy. At least 30 measurements were taken for the bulk and chamfer regions, and at least 15 measurements were taken of the weld region.

Scanning electron microscopy (SEM) and energy dispersive x-ray spectroscopy (EDS) were used to characterize the as received and oxidized (700 °C dry air) EBW tube microstructure. Backscatter and secondary electron images were collected using an accelerating voltage of 20 kV. Map scans of varying sizes, line scans, and point scans were used to characterize the composition of secondary phases present in the microstructure.

2.3. Transient oxidation

As previously stated, TREAT is designed to produce rapid transients with heating rates up to 700 $^{\circ C}/_{s}$ and a relatively slow cooling rate over

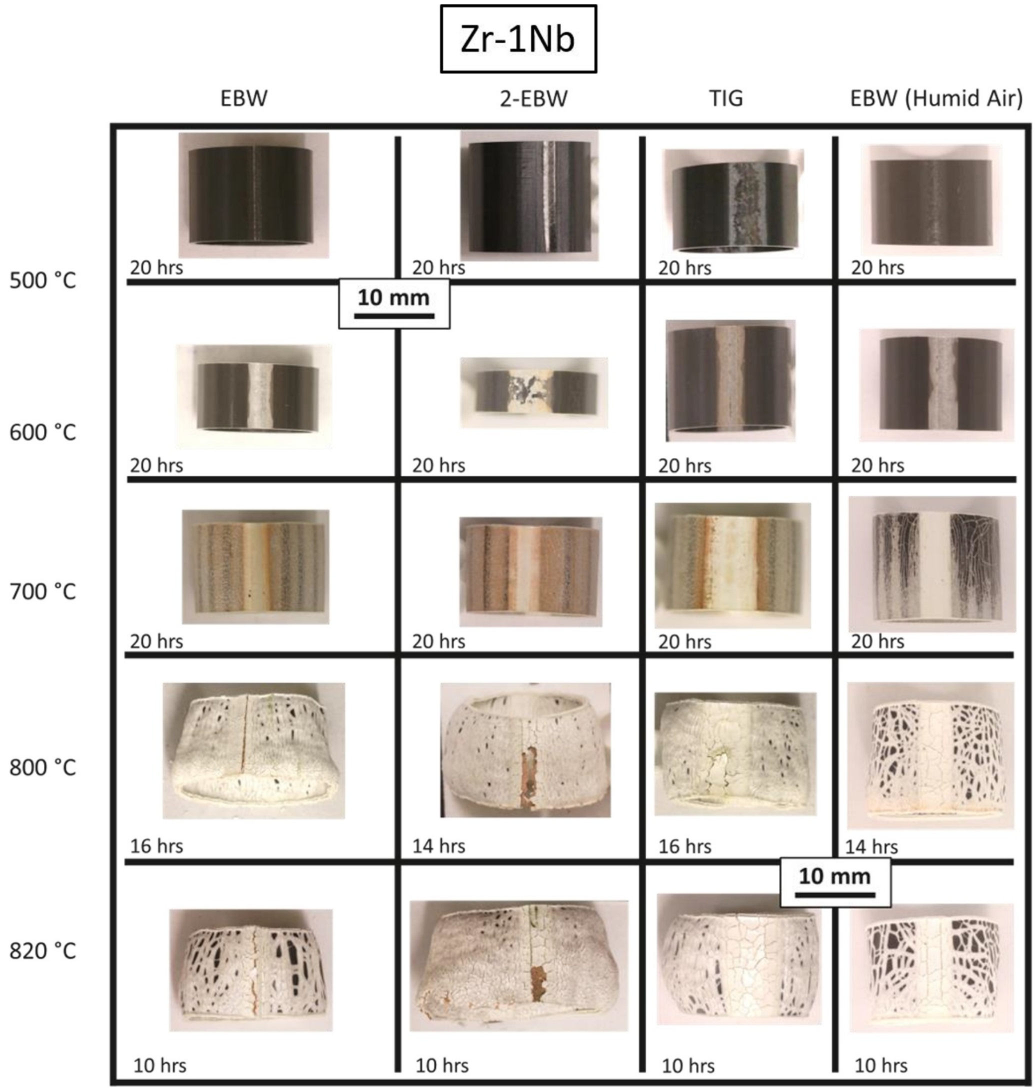

Fig. 7. Macroscopic images of Zr-1Nb EBW or TIG welded tubes after isothermal oxidation experiments in dry or humid air with the weld facing forward.

Table 2
Constants, R^2 values, and calculated activation energies for oxidation of chamfered and welded Zry-3, Zry-4, and Zr–1Nb in air obtained from Arrhenius fits.

		Pre-breakaway			Post-breakaway		
		ln(A)	$-E_a$ ($^{kJ}/_{mol}$)	R^2	ln(A)	$-E_a$ ($^{kJ}/_{mol}$)	R^2
Zry-3	EBW run 1	−0.92	130	0.99	5.27	150	1
	EBW run 2	0.57	140	0.99	4.21	140	0.99
	EBW-2	1.26	150	1	6.81	160	1
	TIG	−0.19	140	1	4.64	140	1
	Humid air	−1.32	130	0.99	5.33	150	0.94
Zry-4	EBW run 1	2.21	160	1	6.65	150	1
	EBW run 2	3.19	160	1	7.29	160	1
	EBW-2	2.84	160	0.99	8.08	170	1
	TIG	0.98	150	0.99	6.73	160	1
	Humid air	0.92	150	1	7.33	160	1
Zr–1Nb	EBW run 1	−0.83	130	0.99	5.50	150	1
	EBW run 2	−3.56	100	0.93	5.41	150	0.99
	EBW-2	3.75	170	0.99	8.10	170	1
	TIG	0.53	140	0.99	6.74	160	1
	Humid Air	0.25	140	0.99	5.87	160	0.99

an extended period of time (10 or more hours to reach room temperature). To replicate these conditions, fifteen transients from 600 to 500 °C (≈600 min of exposure) were completed to simulate normal TREAT operation, followed by a transient from 820 to 450 °C to simulate a DBA scenario. One of the temperature profiles measured from these experiments is shown in Fig. 3. To replicate the transients, a benchtop muffle furnace was heated to the temperature of interest (either 600 or 820 °C) and the specimen was inserted through a port on the top of the furnace. A pure zirconium tube with a thermocouple spot welded onto the surface was inserted simultaneously with the specimen to monitor the temperature (Fig. 4). The experiments were repeated for 2 samples per alloy. The samples were weighed and imaged between each cycle.

3. Results

3.1. Isothermal oxidation

The macroscopic images after isothermal oxidation of EBW and TIG welded zirconium alloys in dry and humid air are shown in Figs. 5–7. The corresponding normalized mass gain data collected during oxidation is shown in Fig. 8. As seen in the mass gain plots, breakaway oxidation occurs in all three alloys at temperatures ≥700 °C and Zry-4

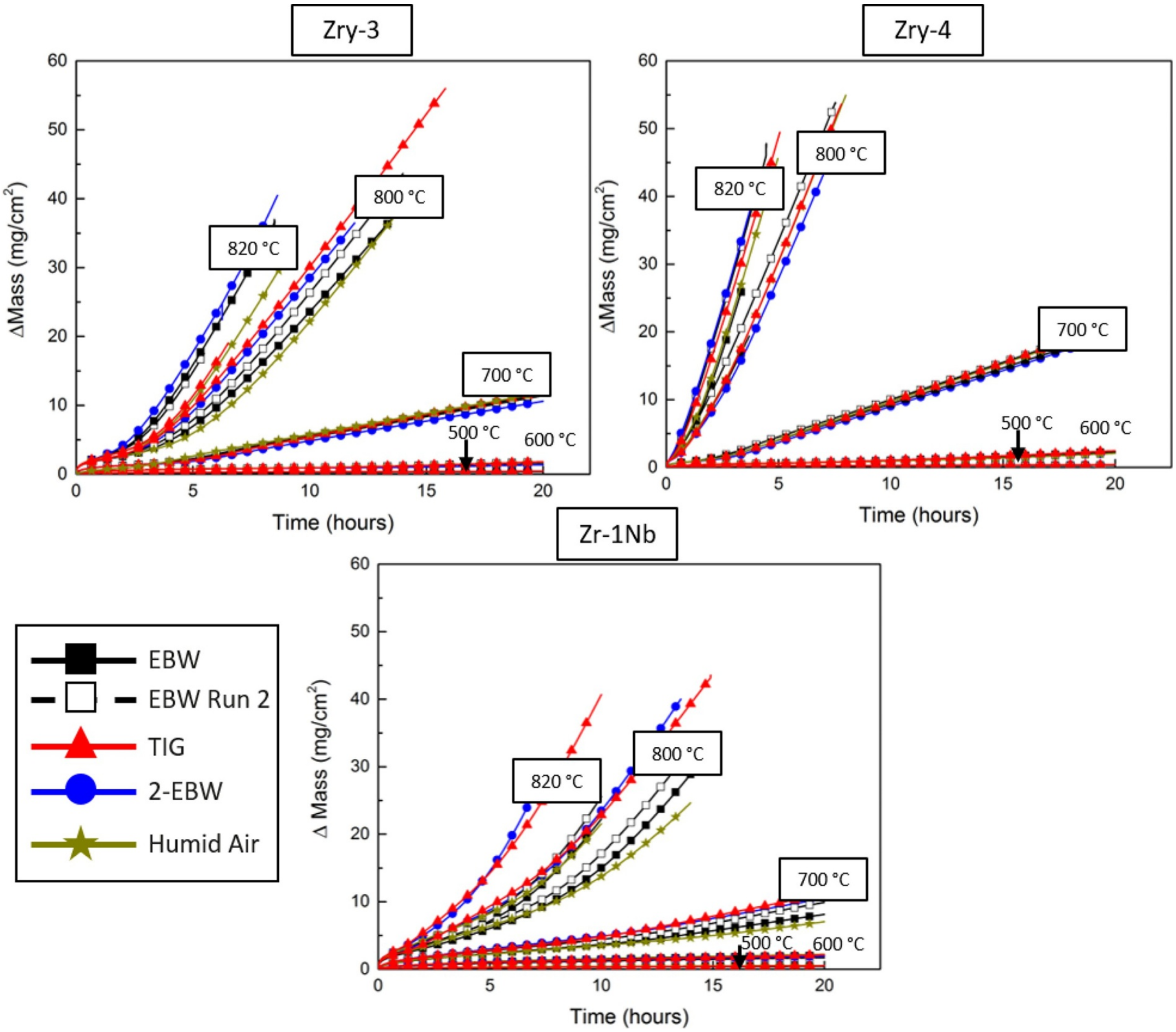

Fig. 8. Mass gain normalized to measured initial surface area during isothermal oxidation experiments of EBW or TIG welded Zry-3, Zry-4, Zr–1Nb tubes in dry or humid air.

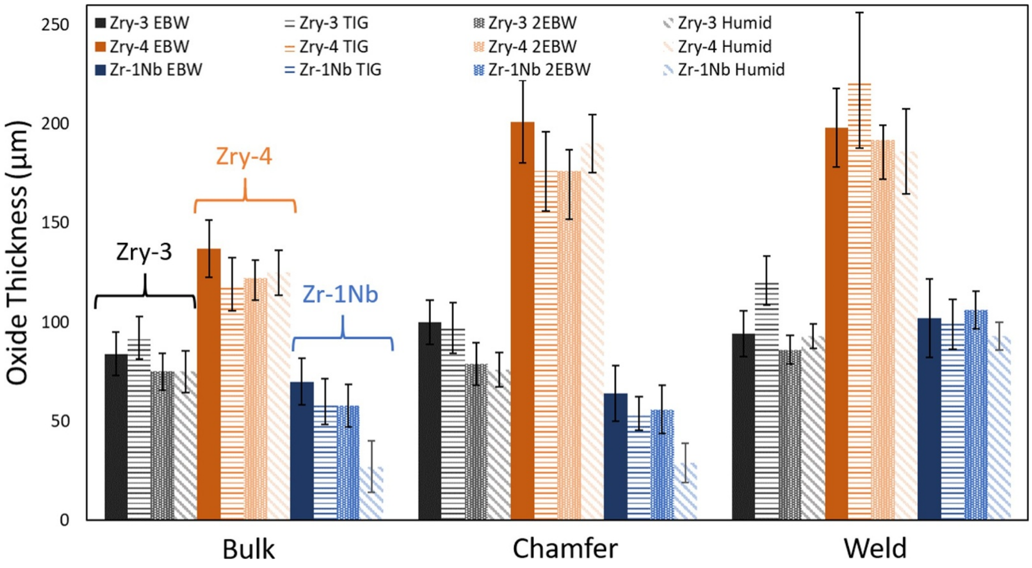

Fig. 9. Oxide thickness of each section of the welded tubes after 20-hour isothermal oxidation at 700 °C. The error bars are the standard deviation of 15 (weld) or 30 (bulk and chamfer) measurements.

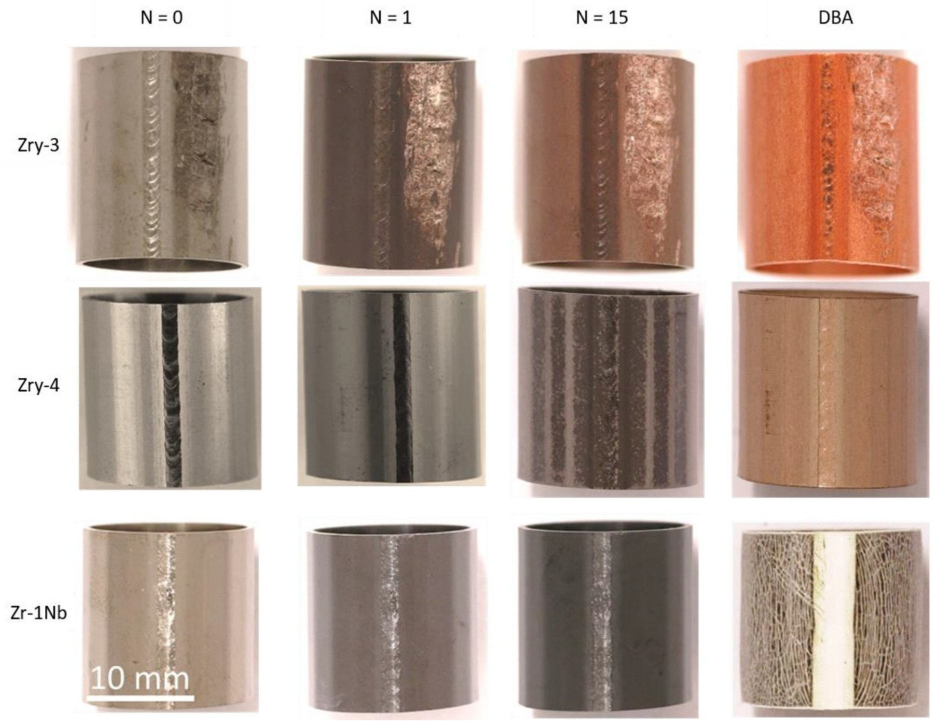

Fig. 10. EBW Zry-3, Zry-4, and Zr–1Nb after $N = 0, 1, 15$ (600 °C) and DBA (820 °C) transient oxidation cycles.

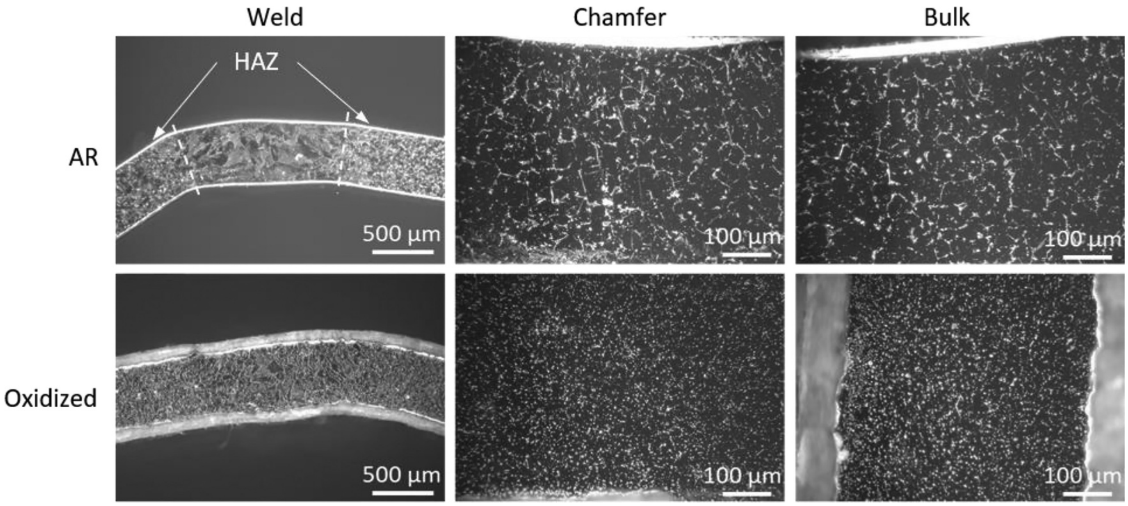

Fig. 11. Dark field optical images of as received (AR) EBW Zry-3 and after 20-h isothermal oxidation at 700 °C in dry air. The microstructure of the weld, chamfered, and bulk regions are shown.

experiences breakaway the earliest of the three alloys, while Zr–1Nb is the most resistant to breakaway.

From Figs. 5–7, and as expected from the discussion above, the HAZ is larger in the TIG welded tubes than in the EBW specimens [18]. The effect of plastic deformation on oxidation behavior is seen in the Sn–Fe containing alloys (Zry-3 and Zry-4); accelerated oxidation on the chamfer regions are clearly visible. In cases where the sample fell apart, the Zry-3 and Zry-4 failed at the chamfers. The opposite is true for the Zr–1Nb alloy; accelerated oxidation occurs first on the non-plastically deformed, or bulk, regions of the tube and fracture occurred at the weld. In contrast to the other two alloys, Zr–1Nb experiences accelerated oxidation in a crack-like network on the surface rather than on the entirety of the surface as seen in the images taken after 800 and 820 °C oxidation. The same behavior was seen during the oxidation of plate specimens [5]. Ballooning occurs in Zry-3 and Zr–1Nb after oxidation ≤800 °C and after oxidation at 820 °C in Zry-4, although most of these samples fell apart at 800 °C making it difficult to determine if ballooning occurred or not. In Zry-4 and Zr–1Nb, the color of the oxide at the weld is noticeably different than the rest of the tube, the weld region being significantly lighter. This difference in color is also seen on Zry-3, however it is less pronounced, particularly on the EBW tubes oxidized at low temperatures.

From the mass gain data in Fig. 8, EBW and TIG welded tubes have similar oxidation kinetics in Zry-4 at all temperatures. The effects of humid air on breakaway oxidation rates, for all specimens, appears insignificant. However, there was a slight difference in oxidation behavior between EBW and TIG welded Zry-3 and Zr–1Nb tubes. The single EBW Zry-3 tube oxidized in both dry and humid air resisted breakaway longer than the TIG welded and 2-EBW tubes during 800 °C oxidation. However, the EBW tube oxidized in humid air and the TIG

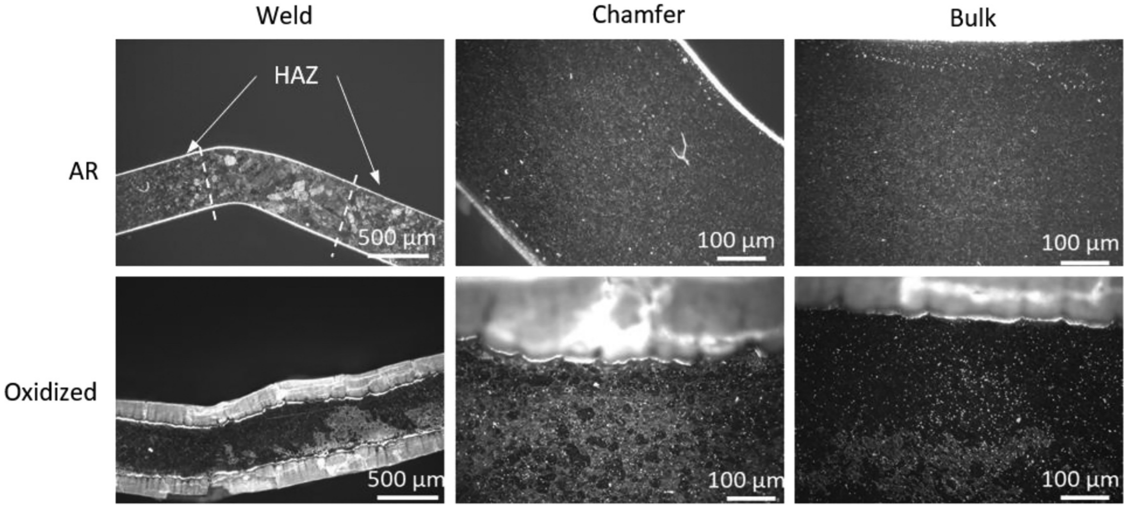

Fig. 12. Dark field optical images of as received (AR) EBW Zry-4 and after 20-h isothermal oxidation at 700 °C in dry air. The microstructure of the weld, chamfered, and bulk regions are shown.

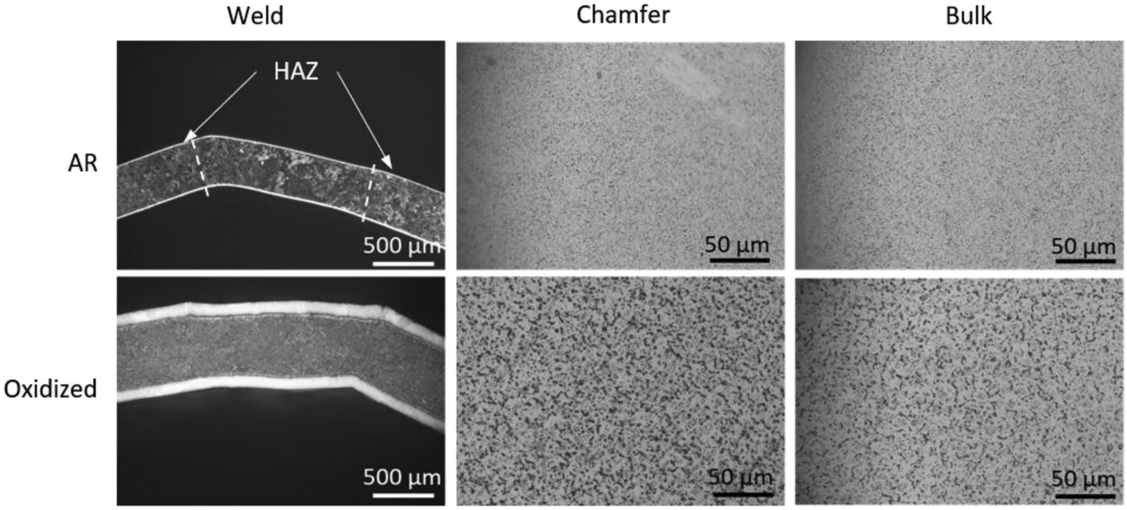

Fig. 13. Dark field (weld) and bright field (chamfer and bulk) optical images of as received (AR) EBW Zr-1Nb and after 20-hour isothermal oxidation at 700 °C in dry air. The microstructure of the weld, chamfered, and bulk regions are shown.

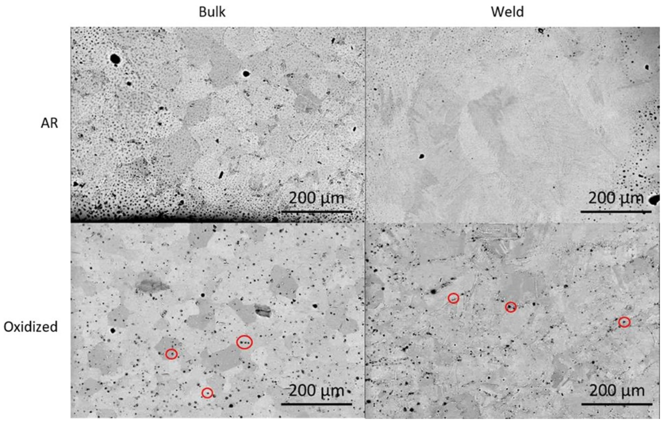

Fig. 14. SEM images of the weld and bulk microstructure of as received (AR) and oxidized (700 °C dry air) EBW Zry-3. All images were collected using backscatter electrons. The circles on the images after oxidation highlight high concentration Fe precipitates.

welded tubes in dry air resisted breakaway the longest at 820 °C. A consistent trend is seen from the mass gain data during oxidation of Zr–1Nb. A difference can be seen in Zr–1Nb at high temperatures, with the single EBW tubes resisting breakaway oxidation longer than the TIG welded tubes.

Fig. 9 shows the average oxide thickness of each specimen after isothermal oxidation at 700 °C. The measurements agree with what is seen in the images of the specimens: the oxidation behavior of Zry-3 is unaffected by chamfering or welding as there is no statistical difference in the oxide thickness between the three regions. The effect of chamfering and welding is clearly seen in Zry-4 (as is visible in Fig. 6 Macroscopic images of Zry-4 EBW or TIG welded tubes after isothermal oxidation experiments in dry or humid air with the weld facing forward.); the chamfer and weld regions are approximately 70% thicker than the bulk regions. Zr–1Nb also exhibits accelerated oxidation at the weld, also clearly visible in Fig. 7, while the bulk and chamfered regions have similar oxide thickness.

3.2. Transient oxidation

Images of the EBW tubes before oxidation ($N = 0$), after the first

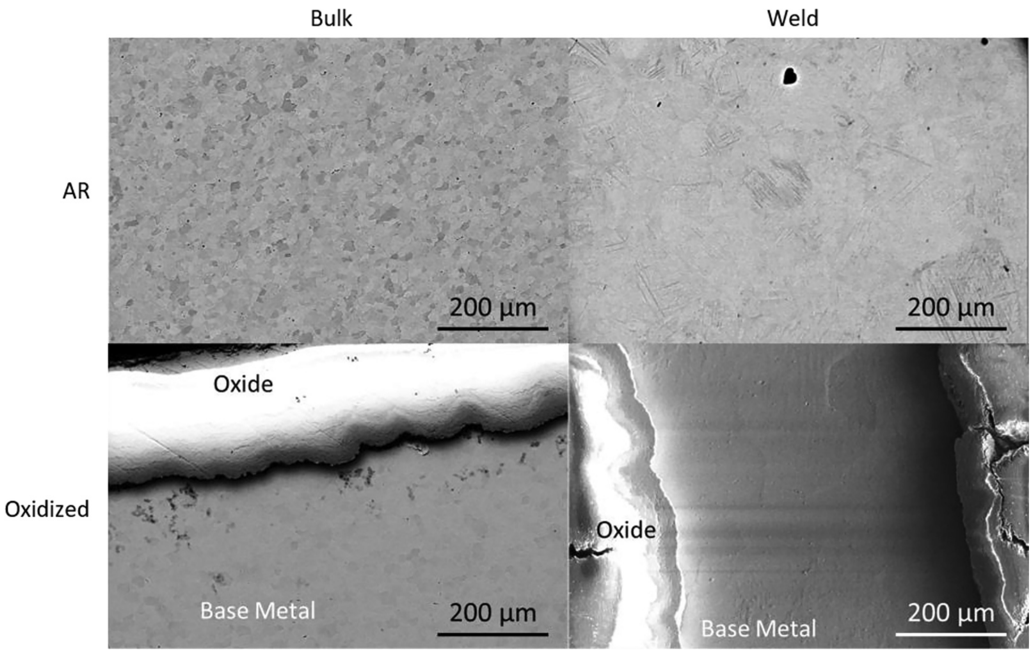

Fig. 15. SEM images of the weld and bulk microstructure of as received (AR) and oxidized (700 °C dry air) EBW Zry-4. All images were collected using backscatter electrons except the oxidized weld region, which is a secondary electron image.

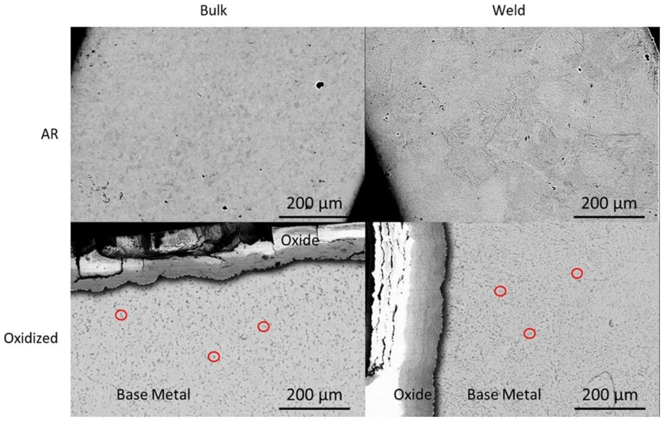

Fig. 16. SEM images of the weld and bulk microstructure of as received (AR) and oxidized (700 °C dry air) EBW Zr–1Nb. All images were collected using backscatter electrons. The circles on the images highlight the Nb and O-rich precipitates identified through EDS.

and fifteenth 600 °C transient cycles ($N = 1$ and $N = 15$) and the final 820 °C transient (*DBA*) are shown in Fig. 10. The behavior of the alloys after transient oxidation is similar to what is seen after isothermal oxidation. Zry-3 and Zry-4 experience accelerated oxidation first on the chamfers (more prominent on Zry-4), while Zr–1Nb maintains its protective oxide until the DBA transient. It should be noted that the as received Zry-3 tube had deformation present next to the weld from the fabrication process (to the right of the weld Fig. 10). The deformation had different surface texture, and therefore different oxidation behavior than the rest of the tube. However, the remainder of the tube was unaffected by the fabrication process, thus observations about the oxidation behavior could be made on most of the tube. After the DBA transient, the characteristic crack-like accelerated oxidation is present along with accelerated oxidation at the weld in Zr-1Nb.

4. Discussion

4.1. General oxidation behavior

The initial oxidation behavior of zirconium alloys is typically characterized by parabolic kinetics, and is governed by diffusion of oxygen anions through the oxide layer [19]. Once the oxide reaches a critical thickness, it cracks and exposes bare metal, which provides a direct path for oxygen to reach the surface. The kinetics then become linear and oxidation occurs very rapidly [4,19]. This transition is termed “breakaway.” The pre- and post-breakaway oxidation kinetics were quantified according to the method presented in a previous publication [5]. The parabolic and linear rate constants for each specimen were determined and then plotted Arrheniusly. The activation energies were calculated from the slope of the curve as discussed in previous work [5]. The activation energies (E_a), constant (A), and variance between the data and linear fit (R^2) both before and after breakaway are in Table 2. The activation energies are rounded to the nearest 10 $^{kJ}/_{mol}$ due to the inherent uncertainty a9sociated with fitting data that is highly dependent on the surface area of the starting material, which is not trivial to measure with the chamfered specimens.

4.2. Effect of welding and plastic deformation on oxidation behavior

It has been shown that the oxidation behavior of zirconium alloys is dependent on the microstructure and secondary phases in the base metal [6–8]. The high temperature of welding alters the microstructure of the zirconium alloys, as is visible in the optical images of the alloys in Figs. 11–13, which shows the microstructure of the EBW bulk, chamfered, and welded regions in the as received material and after 700 °C isothermal oxidation in dry air. The grains in the bulk metal and HAZ are small, equiaxed shaped grains that become increasingly coarser towards the FZ. The FZ exhibits lamellar shaped grains similar to what has been shown in literature [9]. No difference in microstructure is seen between the bulk and chamfered regions in any of the alloys. In Zry-3 (Fig. 11), after oxidation, precipitates appear to be homogeneously dispersed in the non-welded regions. As seen in Fig. 12, no precipitates are visible after oxidation and the microstructure is similar to the as received microstructure. The grains in Zr–1Nb are much smaller than in

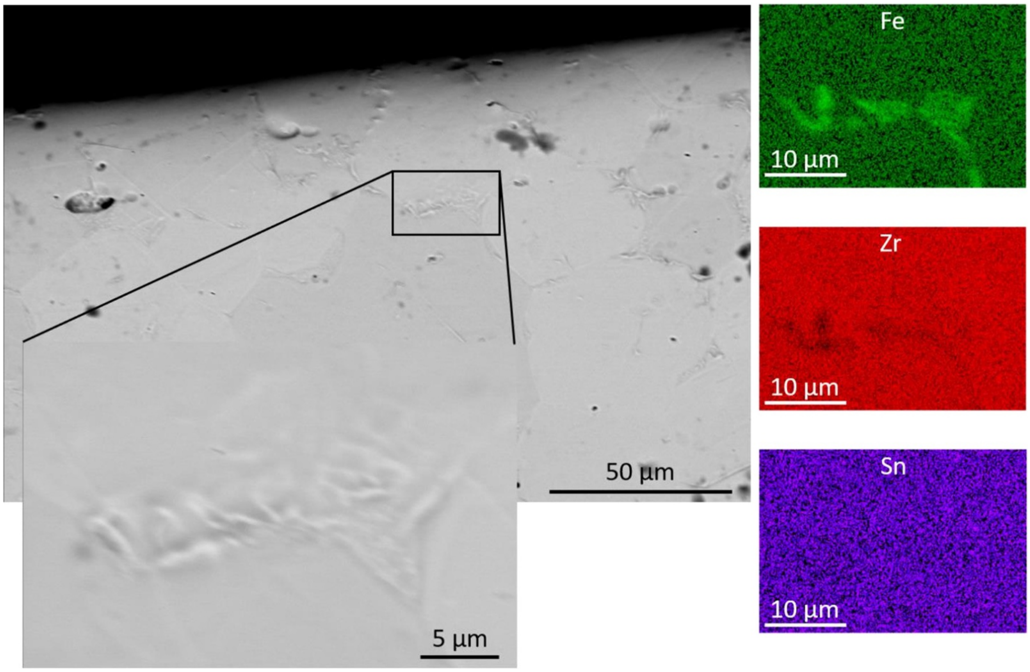

Fig. 17. SEM image and corresponding EDS maps of Fe-rich precipitates found at the grain boundaries of the non-welded regions of as received EBW Zry-3. The intensity of the EDS maps corresponds to concentration of the element in the material.

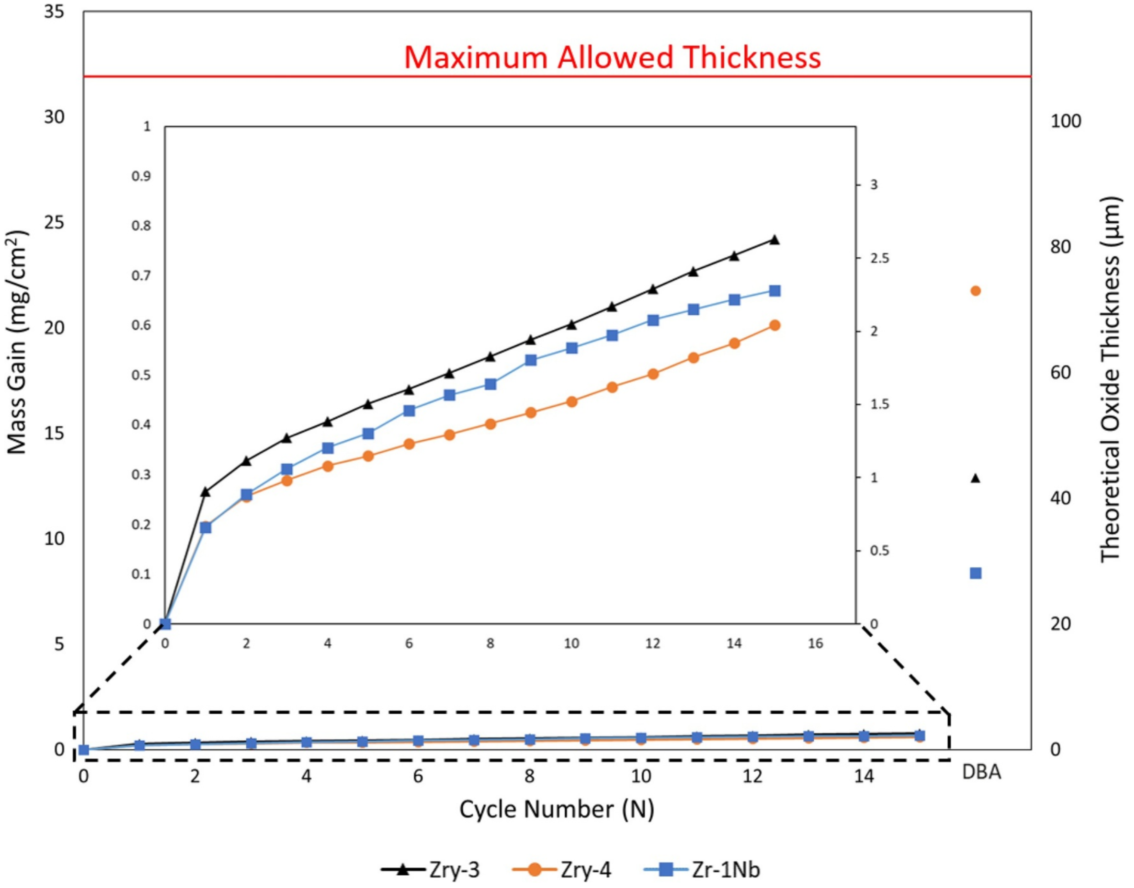

Fig. 18. Average mass gain between runs 1 and 2 and associated theoretical oxide thickness after each 600 °C transient ($N = 1–15$) and after the final 820 °C DBA transient. Maximum allowed oxide thickness (17% of the original wall thickness) is shown for reference. The inset shows a magnified view of the mass gain and theoretical oxide thickness after the 600 °C transients.

the other alloys and are more visible after oxidation, which is likely due to segregation of precipitates at the grain boundaries.

SEM and EDS characterization of the weld and bulk microstructure of the alloys before and after oxidation are shown in Figs. 14–16. Prior to oxidation, no precipitates are present in the welded region of the three alloys. Similar results have been reported for zirconium alloys as a result of EBW [7,9]. It is probable that the temperature achieved during welding was high enough for the precipitates to dissolve into the matrix. The non-welded regions of Zry-3 contained Fe-rich precipitates at the grain boundaries before oxidation, as shown in Fig. 17. These precipitates were found to contain between 2–5% Fe, while the surrounding matrix contained between 0.2–0.4 wt% Sn in solution, as expected from Table 1. No precipitates were found in Zry-4 or Zr–1Nb prior to oxidation. However, it is possible that β-Nb precipitates were present in Zr–1Nb that were too small to be identified via SEM/EDS.

After oxidation, increased Fe precipitation is seen at the grain boundaries in Zry-3 in all regions. Accordingly, the Fe segregation at the grain boundaries seen before oxidation remains, but with a slightly lower Fe concentration (≈ 1 wt%). However, precipitates with much higher Fe concentration (11–13 wt%) formed during oxidation, seen as the dark spots in Fig. 14 (highlighted with circles). Additionally, an approximately 20 μm Fe-depleted region was identified at the metal/oxide interface in both the welded and non-welded regions, where the concentration dropped to nearly 0 wt%. This depleted region was not observed in Zry-4 or Zr–1Nb. During oxidation, Fe segregated to the grain boundaries in the welded region of Zry-4 and had a composition of approximately 0.8 wt% Fe. No precipitates were identified in the non-welded regions (Fig. 15). It has been well characterized that precipitates such as Fe act as nucleation sites for oxidation and can result in stresses and cracks in the oxide, leading to enhanced oxidation [20–22]. The presence of Fe precipitates in the welded region of Zry-4 could contribute to the accelerated oxidation seen in this region. In Zr–1Nb, the precipitates at the grain boundaries after oxidation (some of which are highlighted in Fig. 16) were found to be Nb and O-rich, with some precipitates containing up to 6 wt% Nb. The formation of small Nb precipitates in zirconium alloys has been shown to enhance resistance to breakaway oxidation due to the reduction of supersaturation of Nb in the Zr matrix and stabilization of the tetragonal zirconia phase [17,23]. The resistance to breakaway oxidation of Zr–1Nb is clear from Fig. 8.

4.3. Transient oxidation

The mass gain (normalized to surface area before oxidation) of each specimen during $N = 0\text{–}15$ and DBA transients and theoretical oxide thickness for each alloy is shown in Fig. 18. The data is averaged between 2 runs. Minimal mass gain occurred during transients $N = 1\text{–}15$ and all alloys experienced similar mass gain. After the 820 °C transient, a similar trend appears that was seen during isothermal oxidation: Zry-4 experienced the most mass gain while Zr–1Nb experienced the least after the DBA transient. The maximum allowed thickness is also shown in Fig. 18. This maximum value is defined by the INL as 17% of the original wall thickness of the tube. The thinnest wall thickness (0.635 mm) was used to calculate the maximum oxide thickness shown in Fig. 18 to reflect a conservative value. It is clear that during the 600 °C transients, which is TREAT's maximum normal operating temperature, the oxide thickness is well below the maximum allowed thickness. Even after an 820 °C transient, or accident temperature, all alloys are still well below this maximum thickness. However, the cladding would need to be replaced following a DBA transient to prevent failure during future normal operating conditions.

5. Conclusion

TREAT's cladding is unique in that it has welds, chamfers, and is exposed to rapid transients (700 $^{\circ C}/_{s}$) in air. To study the effect of these conditions on potential cladding material, welded and chamfered Zry-3, Zry-4, and Zr–1Nb tubes have been oxidized under isothermal and transient conditions in both dry and humid air in the temperature range 500–820 °C. Thermogravimetric analysis data was used to quantitatively compare the oxidation behavior between the alloys and weld types. The data was then used to identify the oxidation kinetics of each specimen. Zry-4 was found to be the least resistant to the breakaway transition and oxidized the most rapidly, whereas Zr–1Nb was the most resistant to breakaway. The oxide thickness was measured on the weld, chamfer, and bulk regions of the tubes after 20-h isothermal oxidation at 700 °C and compared. It was found that Zry-4 experiences accelerated oxidation on the chamfered regions which is confirmed by oxide thickness measurements. The oxide thickness is consistent between all three regions in Zry-3 at this temperature; however at temperatures above 700 °C, it is clear that the tubes will fail at either the chamfer or the weld. The oxide on the weld for Zr-1Nb was thicker than the other two regions, which is also seen from the images. Additionally, the oxidation behavior was the same regardless of weld type in Zry-4, while the Zr–1Nb EBW tubes resisted breakaway longer than the TIG welded tubes at temperatures ≤ 700 °C. In Zry-3 at oxidation temperatures ≥ 700 °C, the EBW and TIG welded tubes had similar oxidation kinetics. At 800 °C, the EBW tubes resisted breakaway longer than the TIG welded tubes; however, at 820 °C the TIG welded tubes resisted breakaway the longest.

Comparing the microstructure of the EBW tubes before and after oxidation, it was seen that precipitation of secondary phases occurred in all three alloys during oxidation. After oxidation, Zry-3 and Zry-4 contained Fe-rich precipitates at the grain boundaries. In Zry-3, this occurred in the entire specimen. However, in Zry-4, the precipitation occurred only in the weld region. Zr–1Nb had small Nb-rich precipitates after oxidation. Comparing the microstructure between the weld, chamfer, and bulk regions of the EBW tubes, a clear difference is seen between the welded and non-welded regions. The welded regions consist of lamellar grains that coarsen towards the FZ, while the non-welded regions consist of small, equiaxed grains. The microstructure between the bulk and chamfered regions appear the same.

All three alloys had similar behavior during transient oxidation as in isothermal oxidation. Zry-4 experienced accelerated oxidation on the chamfered regions during the 600 °C transient cycles while Zry-3 only experienced slightly increased oxidation on the chamfers. Zr-1Nb maintained a thin, dense oxide on the entire tube through all 600 °C transients. Additionally, it was determined that after 15 cycles to TREAT's maximum normal operating temperature, followed by an accident type transient to 820 °C, the oxide thickness of all three alloys is still well below ($< 30\%$) the maximum allowed thickness defined by the INL.

Data availability

The raw data required to reproduce these findings are available to download from Mendeley Data. The processed data required to reproduce these findings are available to download from Mendeley Data.

Declaration of Competing Interest

None.

Acknowledgments

The work reported here was funded primarily through Department of Energy's National Nuclear Security Administration (DOE-NNSA) Office of Materials Minimization and Management. The authors would like to thank A. Lupercio and J. Watkins at Boise State University for assistance in performing some of the TGA experiments. The authors would also like to acknowledge B. Forsmann at the Center for Advanced Energy Studies for his help preparing and imaging samples for oxide thickness measurements.

References

[1] J. Carmack, Future transient testing of advanced fuels testing workshop, Report No. INL/EXT-09-16392, Idaho National Laboratory (INL), 2009.

[2] C. Duriez, T. Dupont, B. Schmet, F. Enoch, Zircaloy-4 and M5® high temperature oxidation and nitriding in air, J. Nucl. Mater. 380 (2008) 30–45, https://doi.org/10.1016/j.jnucmat.2008.07.002.

[3] C. Duriez, D. Drouan, G. Pouzadoux, Reaction in air and in nitrogen of pre-oxidised zircaloy-4 and M5™ claddings, J. Nucl. Mater. 441 (2013) 84–95, https://doi.org/10.1016/j.jnucmat.2013.04.095.

[4] M. Steinbrück, S. Schaffer, High-temperature oxidation of zircaloy-4 in oxygen-nitrogen mixtures, Oxid. Met. 85 (2016) 245–262, https://doi.org/10.1007/s11085-015-9572-1.

[5] J.L. Vandegrift, P.M. Price, J.P. Stroud, C.J. Parga, I.J. Van Rooyen, B.J. Jaques, D.P. Butt, Oxidation behavior of zirconium, zircaloy-3, zircaloy-4, zr-1nb, and zr-2.5nb in air and oxygen, Nucl. Mater. Energy (2019), https://doi.org/10.1016/j.nme.2019.100692.

[6] Y.H. Jeong, K. Ok, H.G. Kim, H.G. Jeong, Y.H. Lee, K.O. Kim, Y.H. Jeong, K. Ok, H.G. Kim, Correlation between microstructure and corrosion behavior of Zr–Nb binary alloy, J. Nucl. Mater. 302 (2002) 9–19, https://doi.org/10.1016/S0022-3115(02)00703-1.

[7] C. Cai, L. Li, W. Tao, G. Peng, X. Wang, Weld bead size, microstructure and corrosion behavior of zirconium alloys joints welded by pulsed laser spot welding, J. Mater. Eng. Perform. 25 (2016) 3783–3792, https://doi.org/10.1007/s11665-016-2250-x.

[8] K.Y. Huang, The effect of heat treatment on the microstructure and the corrosion resistance of zircaloy-4 in 450 °C steam, J. Nucl. Mater. 136 (1985) 16–29.

[9] B. Zhang, X. Li, T. Wang, X. Wang, Microstructure and corrosion behavior of Zr-702 joined by electron beam welding, Vacuum 121 (2015) 159–165, https://doi.org/10.1016/j.vacuum.2015.08.005.

[10] C. Cai, W. Tao, L. Li, Y. Chen, Weld bead formation and corrosion behavior of pulsed laser welded zirconium alloy, Int. J. Adv. Manuf. Technol. 77 (2015) 621–628, https://doi.org/10.1007/s00170-014-6474-3.

[11] B.R. Ryabichenko, The corrosion resistance of welded joints in a zirconium-niobium alloy, Autom. Weld 38 (1985) 17–20.

[12] A.Y. Eroshenko, A.M. Mairambekova, Y.P. Sharkeev, Z.G. Kovalevskaya, M.A. Khimich, P.V. Uvarkin, Structure, phase composition and mechanical properties in bioinert zirconium-based alloy after severe plastic deformation, 7 (2017) 469–472.

[13] S.O. Rogachev, S.A. Nikulin, A.B. Rozhnov, M.V. Gorshenkov, Microstructure, phase composition, and thermal stability of two zirconium alloys subjected to high-pressure torsion at different temperatures, Adv. Eng. Mater (2018) 20, https://doi.org/10.1002/adem.201800151.

[14] D. Fuloria, N. Kumar, R. Jayaganthan, S.K. Jha, D. Srivastava, An investigation of effect of annealing at different temperatures on microstructures and bulk textures development in deformed zircaloy-4, Mater. Charact. 129 (2017) 217–233, https://doi.org/10.1016/j.matchar.2017.04.038.

[15] X.Y. Zhang, M.H. Shi, C. Li, N.F. Liu, Y.M. Wei, The influence of grain size on the corrosion resistance of nanocrystalline zirconium metal, Mater. Sci. Eng. A 448 (2007) 259–263, https://doi.org/10.1016/j.msea.2006.10.029.

[16] C.J. Parga, S.K. Varma, Correlation between microstructures and oxidation resistance in Zr–Nb–Ti alloys, Metall. Mater. Trans. A Phys. Metall. Mater. Sci. 40 (2009) 2987–2993, https://doi.org/10.1007/s11661-009-0017-9.

[17] K.N. Choo, Y.H. Kang, S.I. Pyun, V.F. Urbanic, Effect of composition and heat treatment on the microstructure and corrosion behavior of Zr–Nb alloys, J. Nucl. Mater. 209 (1994) 226–235, https://doi.org/10.1111/cpr.12282.

[18] P. Rudling, A. Strasser, F. Garzarolli, Welding of zirconium alloys, 2007.

[19] E. Beuzet, J.S. Lamy, A. Bretault, E. Simoni, Modelling of zry-4 cladding oxidation by air, under severe accident conditions using the MAAP4 code, Nucl. Eng. Des 241 (2011) 1217–1224, https://doi.org/10.1016/j.nucengdes.2010.04.024.

[20] C. Proff, S. Abolhassani, M.M. Dadras, C. Lemaignan, In situ oxidation of zirconium binary alloys by environmental SEM and analysis by AFM, FIB, and TEM, J. Nucl. Mater. 404 (2010) 97–108, https://doi.org/10.1016/j.jnucmat.2010.05.012.

[21] C. Proff, S. Abolhassani, C. Lemaignan, Oxidation behaviour of zirconium alloys and their precipitates – a mechanistic study, J. Nucl. Mater. 432 (2013) 222–238, https://doi.org/10.1016/j.jnucmat.2012.06.026.

[22] B. de Gabory, A.T. Motta, K. Wang, Transmission electron microscopy characterization of zircaloy-4 and zirlotm oxide layers, J. Nucl. Mater. 456 (2015) 272–280, https://doi.org/10.1016/j.jnucmat.2014.09.073.

[23] J.H. Baek, Y.H. Jeong, Breakaway phenomenon of zr-based alloys during a high-temperature oxidation, J. Nucl. Mater. 372 (2008) 152–159, https://doi.org/10.1016/j.jnucmat.2007.02.011.

[24] B. Cox, V.G. Kristsky, C. Lemaignan, V. Polley, I.G. Ritchie, H. Ruhmann, V.N. Shishov, Waterside corrosion of zirconium alloys in nuclear power plants, Vienna, Austria, 1998.